

# Mn(II) Oxidation in Fenton and Fenton Type Systems: Identification of Reaction Efficiency and Reaction Products

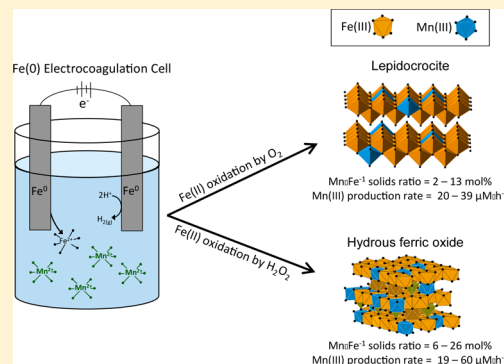
Case M. van Genuchten<sup>†,‡</sup> and Jasquelin Peña<sup>\*,†,§</sup>

<sup>†</sup>Institute of Earth Surface Dynamics, University of Lausanne, Lausanne CH-1015, Switzerland

<sup>‡</sup>Department of Earth Sciences, Geochemistry, Faculty of Geosciences, Utrecht University, Utrecht 3508TA, The Netherlands

## Supporting Information

**ABSTRACT:** Efficient and low-cost methods of removing aqueous Mn(II) are required to improve the quality of impacted groundwater supplies. In this work, we show that Fe(0) electrocoagulation (EC) permits the oxidative removal of Mn(II) from solution by reaction with the reactive oxidant species produced through Fe(II) oxidation. Manganese(II) removal was enhanced when the accumulation of aqueous Fe(II) was minimized, which was achieved at low Fe(II) production rates, high pH, the presence of H<sub>2</sub>O<sub>2</sub> instead of O<sub>2</sub> as the initial Fe(II) oxidant, or a combination of all three. In addition, in the EC–H<sub>2</sub>O<sub>2</sub> system, Mn(II) removal efficiency increased as pH decreased from 6.5 to 4.5 and as pH increased from 6.5 to 8.5, which implicates different reactive oxidants in acidic and alkaline solutions. Chemical analyses and X-ray absorption spectroscopy revealed that Mn(II) removal during Fe(0) EC leads to the formation of Mn(III) (0.02 to >0.26 Mn·Fe<sup>−1</sup> molar ratios) and its incorporation into the resulting Fe(III) coprecipitates (lepidocrocite and hydrous ferric oxide for EC–O<sub>2</sub> and EC–H<sub>2</sub>O<sub>2</sub>, respectively), regardless of pH and Fe(II) production rate. The Mn(II) oxidation pathways elucidated in this study set the framework to develop kinetic models on the impact of Mn(II) during EC treatment and in other Fenton type systems.



## INTRODUCTION

The oxidation of aqueous divalent manganese (Mn(II)) to form insoluble Mn(III,IV) oxides is relevant in the contexts of drinking water treatment and environmental geochemistry. For example, in raw drinking water in which the Mn(II) concentrations can surpass several milligrams per liter,<sup>1,2</sup> Mn(II) is commonly removed to the solid phase via chemical or biological oxidation to address aesthetic water-quality concerns.<sup>3</sup> However, recent evidence suggests that chronic exposure to Mn(II) in drinking water may be associated with neurological effects and thus require more stringent regulation than the current United States Environmental Protection Agency and World Health Organization regulatory recommendation of 50 μg·L<sup>−1</sup>.<sup>4–8</sup> In natural systems, the oxidation of Mn(II) leads to the formation of nanocrystalline Mn(III,IV) oxides, which can act as potent oxidants for elements like arsenic (As), chromium (Cr), and cobalt (Co) as well as natural organic matter and organic contaminants.<sup>9–12</sup> For these reasons, the pathways of Mn(II) oxidation have been studied extensively.<sup>3,13–15</sup>

The oxidation of Mn(II) by O<sub>2</sub> is thermodynamically favorable; however, this reaction is strongly kinetically limited, even in the presence of mineral surfaces at circumneutral pH values.<sup>16,17</sup> Therefore, Mn(II) oxidation in engineered and natural systems requires biological or chemical catalysis. In drinking water treatment, Mn(II) removal is achieved through adsorption,<sup>18</sup> membrane filtration,<sup>19</sup> or by oxidation using

strong oxidants such as permanganate (MnO<sub>4</sub><sup>−</sup>)<sup>20</sup> and ozone (O<sub>3</sub>)<sup>21</sup> or via biological processes,<sup>3</sup> whereas in natural systems, enzymatic Mn(III,IV) production via microorganisms is recognized as the dominant Mn(II) oxidation pathway.<sup>9</sup> However, recent work shows that Mn(II) can also be oxidized by reactive intermediates like superoxide radical (·O<sub>2</sub><sup>−</sup>) produced from photochemical reactions with organic carbon or from extracellular microbiological processes.<sup>14,15,22,23</sup> Therefore, reactive intermediates, including ·O<sub>2</sub><sup>−</sup>, may represent a viable and efficient pathway for Mn(II) oxidation. Other reactive intermediates including hydroxyl radical (·OH) or the ferryl ion (Fe(IV)) may play a similar role in Mn(II) oxidation;<sup>24,25</sup> however, these reactions have received little attention.

Powerful, short-lived oxidants, including ·O<sub>2</sub><sup>−</sup> and ·OH at acidic pH, and presumably an Fe(IV) species at circumneutral pH<sup>26,27</sup> are generated by the oxidation of Fe(II) by O<sub>2</sub> (modified Fenton reaction) or by the oxidation of Fe(II) by H<sub>2</sub>O<sub>2</sub> (Fenton reaction). On the basis of the known pathways of Fe(II)-mediated reactive oxidant production, we expect that Mn(II) can be oxidized by both ·O<sub>2</sub><sup>−</sup> and the intermediate produced from Fe(II) oxidation by H<sub>2</sub>O<sub>2</sub> (see Figure 1).<sup>26,28,29</sup>

Received: November 7, 2016

Revised: January 30, 2017

Accepted: January 31, 2017

Published: January 31, 2017

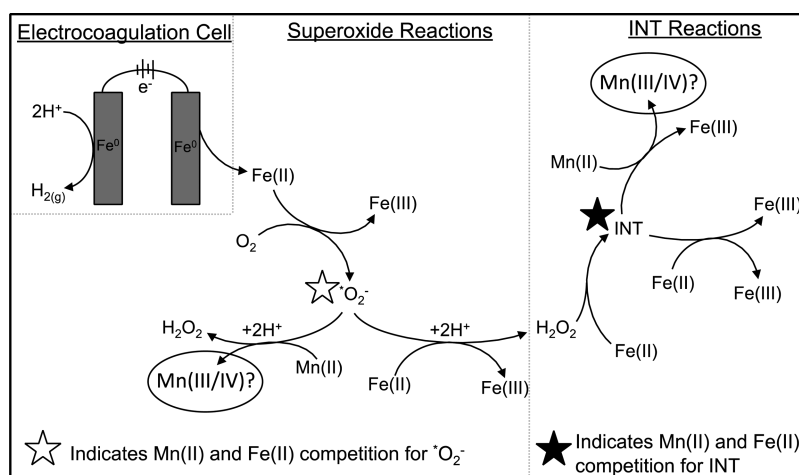


**Figure 1.** Proposed pathways of Fe(II)-mediated Mn(II) oxidation in the EC system following Hug et al. (2003) and Li et al. (2012). In this schematic, the oxidant produced via Fe(II) oxidation by  $\text{H}_2\text{O}_2$  is indicated by INT, which varies with pH;  $\cdot\text{OH}$  is produced at acidic pH, whereas Fe(IV) likely forms at circumneutral pH.

These modified Fenton and Fenton reactions (together, defined as Fenton type reactions in this work) have well-documented applications in water and wastewater treatment<sup>30–32</sup> and are important to contaminant dynamics and soil organic matter decomposition.<sup>33,34</sup> In particular, Fenton type reactions underpin the efficiency of a variety of Fe-based As(III) removal technologies, including Fe(0) electrocoagulation (EC),<sup>35</sup> chemical coagulation with ferrous salts,<sup>36</sup> and zerovalent iron (ZVI) filters.<sup>37</sup> The efficiencies of these systems hinge on maximizing the extent of As(III) oxidation to As(V).<sup>38</sup> For example, optimal As removal in an Fe(0) EC system was observed when the accumulation of aqueous Fe(II), which competes with As(III) for Fenton type products, was minimized.<sup>29</sup> By extension, the concentration of Fe(II) in Fenton type systems may modulate the extent and pathway of Mn(II) oxidation.

In this work, our objectives are to determine the efficiency of Fe(II)-mediated Mn(II) oxidation in an Fe(0) EC system and to identify the reaction products. We measured the kinetics of Mn(II) oxidation in an Fe(0) EC system, which is based on the production of Fe(II) ions via an electric current applied to Fe(0) electrodes.<sup>29,39</sup> Iron EC provides precise control on the rate of Fe(II) production and, therefore, user control on the production of Fenton type products.<sup>29</sup> We measured Mn(II) oxidation efficiency as a function of several parameters: the iron(II) production rate (IPR), solution pH, and the initial Fe(II) oxidant (i.e.,  $\text{O}_2$  versus  $\text{H}_2\text{O}_2$ ). Kinetic experiments were coupled with (i) pyrophosphate extractions to quantify the production of Mn(III) and (ii) X-ray absorption spectroscopy (XAS) at the Mn and Fe K-edges to provide average Mn oxidation number and local Mn and Fe coordination environments, which we used to characterize the reaction products. The Mn(II) oxidation pathways elucidated in our study provide a framework to model the impact of Mn(II) in Fenton type systems.

## MATERIALS AND METHODS

**Kinetics of Mn(II) Removal.** The configuration of the Fe(0) EC cell used for kinetic experiments is described elsewhere.<sup>40,41</sup> The electrolyte (200 to 250 mL) for each experiment consisted of 100  $\mu\text{M}$  initial  $\text{MnCl}_2$  in air-saturated 18 M $\Omega$ -cm deionized (DI) water. Experiments in the EC– $\text{O}_2$

system were performed only at pH 7.5 and 8.5 due to the slow kinetics of Fe(II) oxidation by  $\text{O}_2$  at acidic pH values ( $k_{\text{app}} \approx 10^{-6} \text{ s}^{-1}$  at  $\text{pH} < 5$ ).<sup>42,43</sup> In the EC– $\text{H}_2\text{O}_2$  system, which contained 250  $\mu\text{M}$  initial  $\text{H}_2\text{O}_2$ , experiments were performed at pH values of 4.5 to 8.5 in 1 pH unit increments, with experiments at 4.5 and 5.5 carried out in a 2 mM NaCl background electrolyte and experiments at  $\text{pH} > 5.5$  carried out in a 2 mM  $\text{NaHCO}_3$  buffer.<sup>29,44</sup> Solution pH was controlled by bubbling  $\text{CO}_2(\text{g})$  for experiments in  $\text{NaHCO}_3$  buffer or by small additions of dilute HCl or NaOH for experiments in NaCl. Prior to electrolysis, an aliquot of the electrolyte was acidified (2%  $\text{HNO}_3$ ) to measure the initial Mn concentration by inductively coupled plasma optical emission spectrometry (ICP-OES, PerkinElmer Optima 8300).

Manganese(II) removal experiments were initiated by applying galvanostatic currents of 5 to 33 mA (current densities of 0.4 to 2.8  $\text{mA}\cdot\text{cm}^{-2}$ ) to the EC cell open to the atmosphere. According to Faraday's law, this range of currents corresponds to iron(II) production rates (IPR) of approximately 5–50  $\mu\text{M}\cdot\text{min}^{-1}$ . Based on these IPR values, the electrolysis time to generate the total dosed Fe(II) (170 to 200  $\mu\text{M}$ ) was determined to be 4 min at the highest IPR and 35 min at the lowest IPR. During electrolysis, aliquots of the suspension were sampled at 25, 50, 75 and 100% of the total Fe(II) dosed, filtered immediately, and acidified (2%  $\text{HNO}_3$ ) for ICP-OES measurements of Fe and Mn in the filtrate. The removal of Mn(II) was calculated as the difference between the Mn concentration in the initial electrolyte and filtered suspension. An aliquot of the final suspension was also acidified to measure the total dosed Fe by ICP-OES. We define the Mn(II) removal efficiency ( $\text{mol}\cdot\text{mol}^{-1}$ ) as the mol of Mn(II) removed per mol of Fe(II) added, whereas the Mn(II) removal rate ( $\mu\text{M}\cdot\text{min}^{-1}$ ) is defined as the concentration of Mn(II) removed per time.

Finally, we performed additional experiments to determine the extent of Mn(II) sorption and oxidation by ferrihydrite. In these experiments, 200  $\mu\text{M}$  Fe(III) was added as freshly prepared ferrihydrite<sup>45</sup> to electrolytes with identical solution composition as the EC experiments. A 35 min reaction time was selected to match the longest EC experiment. Aliquots of the control suspensions were taken throughout the reaction, filtered immediately, and acidified for Mn and Fe measurements by ICP-OES.

**Pyrophosphate Extractions.** The production of Mn(III) in all experiments was quantified by Na-pyrophosphate (PP) extraction and UV-vis spectrophotometry.<sup>46</sup> Because Mn(III)-PP ( $\epsilon_{\text{Mn}} = 6.6 \times 10^{-3} \text{ L} \cdot (\mu\text{mol} \cdot \text{cm})^{-1}$ ) and Fe(III)-PP ( $\epsilon_{\text{Fe}} = 3.2 \times 10^{-3} \text{ L} \cdot (\mu\text{mol} \cdot \text{cm})^{-1}$ ) complexes absorb light at 254 nm, we corrected all absorbance measurements according to  $\text{Abs}_{\text{Mn(III)}} = \text{Abs}_{\text{TOT}} - \text{Abs}_{\text{Fe(III)}} = \text{Abs}_{\text{TOT}} - \text{Fe}_{\text{ICP}} \cdot \epsilon_{\text{Fe(III)}}$ , where  $\text{Abs}_{\text{TOT}}$  is the total absorption,  $\text{Abs}_{\text{Fe(III)}}$  is the absorption due to Fe(III)-PP, and  $\text{Fe}_{\text{ICP}}$  is the total Fe concentration measured independently via ICP-OES. The Mn(III) concentration was then calculated according to  $[\text{Mn(III)}] = \text{Abs}_{\text{Mn(III)}} / \epsilon_{\text{Mn(III)}}$ . This approach assumes all Fe present in the solids is Fe(III), which is consistent with previous work.<sup>29,35</sup> A detailed description of this approach is given in the [Supporting Information](#).

**X-ray Absorption Spectroscopy. Data Collection and Reduction.** Mn and Fe K-edge XAS data were collected at the European Synchrotron Radiation Facility (ESRF, BM-01 and BM-23) and the Stanford Synchrotron Radiation Lightsource (BL 4-1 and 11-2). Mn K-edge XAS data were collected in fluorescence mode and calibrated to a Mn foil (6539 eV) up to a reciprocal space value of 11.7–12.0  $\text{\AA}^{-1}$  using a solid-state passivated implanted planar silicon (PIPS) detector, Lytle detector with Soller slits, or Ge detector. Fe K-edge XAS data were collected in transmission mode calibrated to a Fe foil (7112 eV) up to a reciprocal space value 12.5–13.0  $\text{\AA}^{-1}$  using ion chambers for measurements of  $I_0$  and  $I_t$ . Data reduction followed standard procedures. Additional information on XAS is given in the [Supporting Information](#).

**XANES Analysis.** The fraction of Mn(II), Mn(III), and Mn(IV) in EC samples was quantified by linear combination fits (LCF) using Sixpack software.<sup>47</sup> The normalized XANES spectra were fit from 6530 to 6590 eV using Mn(II)-, Mn(III)-, and Mn(IV)-bearing reference compounds. Previous work has shown that the Mn(II), Mn(III), and Mn(IV) fractions derived from XANES LCFs can depend on the nature of the reference compound used in the fit.<sup>48</sup> To minimize artifacts from the choice of reference compound, we performed four different fits for each experimental spectrum using different combinations of five Mn references obtained from previous studies<sup>46,48</sup> or as part of this work: aqueous Mn(II), manganite ( $\gamma\text{-MnOOH}$ ), bixbyite ( $\alpha\text{-Mn}_2\text{O}_3$ ),  $\delta\text{-MnO}_2$ , and ramsdellite ( $\beta\text{-MnO}_2$ ). Following previous approaches,<sup>48</sup> negative fit-derived fractions were not permitted in the fit, but we allowed the sum of components to vary (sums were always  $>0.9$ , with most  $>0.95$ ). The fraction of Mn(II), Mn(III), and Mn(IV) in the samples were then calculated by taking the average and standard deviation of the results of the four LCFs for each sample. Finally, the Mn(III) content in the solid phase was calculated by multiplying the LCF-derived percent Mn(III) by the total concentration of the Mn(II) removed from solution as determined by ICP-OES.

**EXAFS Analysis.** Shell-by-shell fits of the Fe and Mn K-edge EXAFS spectra from representative samples in the EC- $\text{O}_2$  and EC- $\text{H}_2\text{O}_2$  systems were performed in  $R+\Delta R$ -space ( $\text{\AA}$ ) using the SixPack software,<sup>47</sup> which is built on algorithms derived from the IFEFFIT library.<sup>49</sup> Phase and amplitude functions for single scattering paths (Fe-O, Fe-Fe, Mn-O, Mn-Mn/Fe) were calculated using FEFF6<sup>50</sup> based on the structures of goethite ( $\alpha\text{-FeOOH}$ )<sup>51</sup> and birnessite ( $\text{MnO}_2$ ).<sup>52</sup> Due to the similar atomic numbers of Fe and Mn, these two backscattering atoms cannot be distinguished in shell-by-shell fits of the EXAFS spectra. Therefore, we report our second-shell fitting

results as  $\text{CN}_{\text{Mn-Mn/Fe}}$  and  $\text{R}_{\text{Mn-Mn/Fe}}$ . Additional details are provided in the [Supporting Information](#).

## RESULTS

**Time-Dependent Mn(II) Removal. Effect of IPR and pH in the Modified Fenton System.** Figure 2A,B shows the

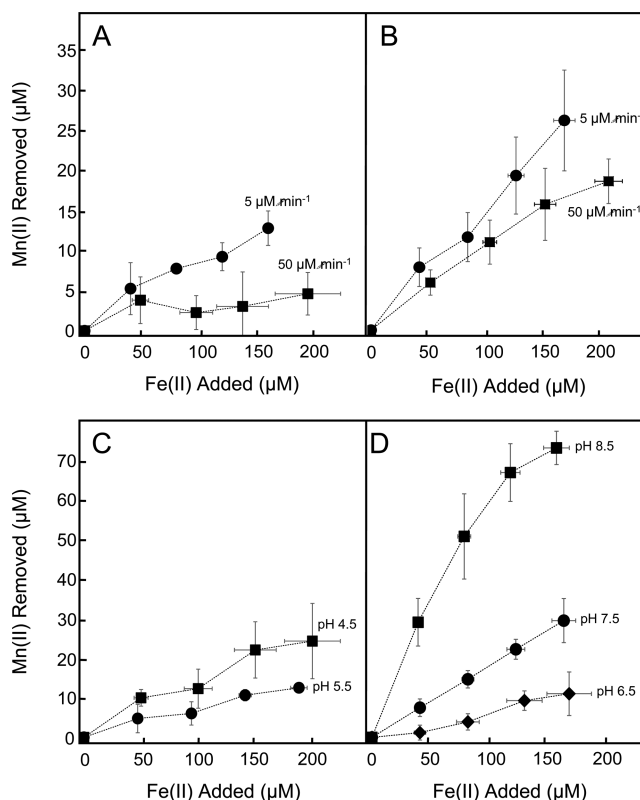


**Figure 2.** Removal of Mn(II) as a function of Fe(II) added in the EC- $\text{O}_2$  (A and B) and EC- $\text{H}_2\text{O}_2$  (C and D) systems. Panels A and B show the effect of IPR at pH 7.5 (A) and 8.5 (B) in the EC- $\text{O}_2$  system, with the circles and squares representing IPR values of 5 and 50  $\mu\text{M} \cdot \text{min}^{-1}$ , respectively. Panels C and D show the removal of Mn(II) as a function of Fe(II) added in the EC- $\text{H}_2\text{O}_2$  system at pH 4.5 and 5.5 (C) and 6.5 to 8.5 (D). In panels C and D, the IPR was 5  $\mu\text{M} \cdot \text{min}^{-1}$ . All data points represent the average and standard deviation of experiments performed at least in triplicate. The lines between data points serve only to guide the eye.

removal of Mn(II) in the EC- $\text{O}_2$  system at pH 7.5 and 8.5, respectively, for two different iron production rates (IPR = 5 and 50  $\mu\text{M} \cdot \text{min}^{-1}$ ). Manganese(II) removal increases with increasing pH and decreasing IPR. However, the IPR influenced Mn(II) removal differently at the two pH values tested. At pH 7.5, the amount of Mn(II) removed from solution increases substantially with decreasing IPR. When normalized by the amount of Fe(II) added, the Mn(II) removal efficiency (mol Mn(II) removed per mol Fe(II) added) is about 4 times greater when Fe(II) is added at 5  $\mu\text{M} \cdot \text{min}^{-1}$  (0.08 mol·mol<sup>-1</sup>) than at 50  $\mu\text{M} \cdot \text{min}^{-1}$  (0.02 mol·mol<sup>-1</sup>). In contrast, at pH 8.5, Mn(II) removal is only slightly improved by a 10-fold decrease in IPR (Figure 2B). If the Fe(II) added is converted to electrolysis time by dividing by the IPR (5.5 and 50  $\mu\text{M} \cdot \text{min}^{-1}$ ), Mn(II) removal rates of 23–70  $\mu\text{M} \cdot \text{h}^{-1}$  at pH 7.5 and 48–280  $\mu\text{M} \cdot \text{h}^{-1}$  at pH 8.5 are obtained.

**Effect of pH in the Fenton System.** Figure 2C,D illustrates the effect of pH on Mn(II) removal in the EC- $\text{H}_2\text{O}_2$  system.



All data shown in Figures 2C,D were generated at an IPR of  $5 \mu\text{M}\cdot\text{min}^{-1}$ . The comparison of Mn(II) removal at pH 7.5 and 8.5 across the EC–O<sub>2</sub> (Figure 2A,B) and EC–H<sub>2</sub>O<sub>2</sub> systems (Figures 2C,D) shows that the Mn(II) removal efficiency is considerably greater when Fe(II) is oxidized by H<sub>2</sub>O<sub>2</sub> relative to O<sub>2</sub>. For example, Mn(II) removal efficiency at pH 7.5 increased from 0.08 to 0.18 mol·mol<sup>−1</sup> when the Fe(II) oxidant was changed from O<sub>2</sub> to H<sub>2</sub>O<sub>2</sub>. Lower IPR values improved Mn(II) removal efficiency in the EC–H<sub>2</sub>O<sub>2</sub> system (1.8 to 2.4-fold increase as IPR was decreased from 50 to  $5 \mu\text{M}\cdot\text{min}^{-1}$ , data not shown) but to a lesser extent than the EC–O<sub>2</sub> system.

Because Fe(II) is oxidized rapidly by H<sub>2</sub>O<sub>2</sub> over a wide range of pH values,<sup>26,42</sup> significant Mn(II) removal was observed from 4.5 to 8.5 in the EC–H<sub>2</sub>O<sub>2</sub> system. However, the relationship between Mn(II) removal and pH was U-shaped. Although Mn(II) removal decreased as pH decreased from 8.5 to 6.5, this trend reverses as pH decreased from 6.5 to 4.5. As a result, the lowest Mn(II) removal efficiency ( $0.06 \text{ mol}\cdot\text{mol}^{-1}$ ) in the EC–H<sub>2</sub>O<sub>2</sub> system was measured at pH 6.5, with roughly twice as efficient Mn(II) removal observed as pH decreased to 4.5 ( $0.12 \text{ mol}\cdot\text{mol}^{-1}$ ).

**Mn(II) Removal in Ferrihydrite Controls.** Consistent with previous research,<sup>53</sup> we found no Mn(II) sorption at pH values below 7.5, but approximately  $0.06$  and  $0.18 \text{ mol Mn(II)}\cdot\text{mol}^{-1} \text{ Fe}$  were removed after 35 min of reaction in the ferrihydrite–O<sub>2</sub> and ferrihydrite–H<sub>2</sub>O<sub>2</sub> experiments, respectively, conducted at pH 8.5. This result indicates that Mn(II) sorption to Fe(III) precipitates generated in EC experiments at pH  $\leq 7.5$  is negligible. At pH 8.5, the production of Mn(III) ( $\approx 30 \mu\text{M}$ ) was only measured in the ferrihydrite–H<sub>2</sub>O<sub>2</sub> system (detection limit near  $6 \mu\text{M Mn(III)}$ ; see the Supporting Information). The presence of H<sub>2</sub>O<sub>2</sub> led to a Mn(III)·Fe<sup>−1</sup> ratio of  $0.12 \text{ mol}\cdot\text{mol}^{-1}$  in the suspension at the end of the 35 min reaction (Figure S3, Table S1). These results suggest that surface catalyzed oxidation of Mn(II) by H<sub>2</sub>O<sub>2</sub> may account for up to  $0.12 \text{ mol}\cdot\text{mol}^{-1}$  of the Mn(II) removed in the EC–H<sub>2</sub>O<sub>2</sub> experiments at pH 8.5, which showed a total removal of  $0.38 \text{ mol}\cdot\text{mol}^{-1}$ . However, we note that this  $0.12 \text{ mol}\cdot\text{mol}^{-1}$  value is likely an overestimation of the surface-catalyzed Mn(II) oxidation in the EC–H<sub>2</sub>O<sub>2</sub> sample at pH 8.5 because the contact time of the solid Fe(III) precipitates with Mn(II) in the EC experiments is lower than in the ferrihydrite controls.

**Manganese Valence in Reaction Products. Pyrophosphate Extractions.** In Figure 3, we plot the Mn(III)·Fe<sup>−1</sup> molar ratio derived from pyrophosphate (PP) extractions and from XANES LCFs for EC–O<sub>2</sub> and EC–H<sub>2</sub>O<sub>2</sub> experiments (IPR =  $5 \mu\text{M}\cdot\text{min}^{-1}$ ) as a function of pH. The PP extractions (filled circles) show that the pH dependence of Mn(III) production in the EC–O<sub>2</sub> and EC–H<sub>2</sub>O<sub>2</sub> systems follows the same trend as that observed for Mn(II) removal. In the EC–O<sub>2</sub> system, the Mn(III)·Fe<sup>−1</sup> ratio increases from 0.06 to  $0.10 \text{ mol}\cdot\text{mol}^{-1}$  as pH increased from 7.5 to 8.5. The data in the EC–H<sub>2</sub>O<sub>2</sub> system, which were corrected for surface-catalyzed Mn(III) production at pH 8.5 (both PP extractions and XANES-derived data were corrected), show a nearly linear increase in the Mn(III)·Fe<sup>−1</sup> ratio from 0.06 to  $0.26 \text{ mol}\cdot\text{mol}^{-1}$  as pH increased from 6.5 to 8.5. Decreasing pH from 6.5 to 4.5 increased the Mn(III)·Fe<sup>−1</sup> ratio from 0.06 to  $0.13 \text{ mol}\cdot\text{mol}^{-1}$ .

**Mn K-Edge XANES.** Linear combination fits of the Mn K-edge XANES spectra of the solid reaction products confirm that Mn in the solid phase is present dominantly as Mn(III) regardless of pH and the initial presence or absence of H<sub>2</sub>O<sub>2</sub> (Figure S5). The LCFs returned a percent Mn(III) of  $89 \pm 12$

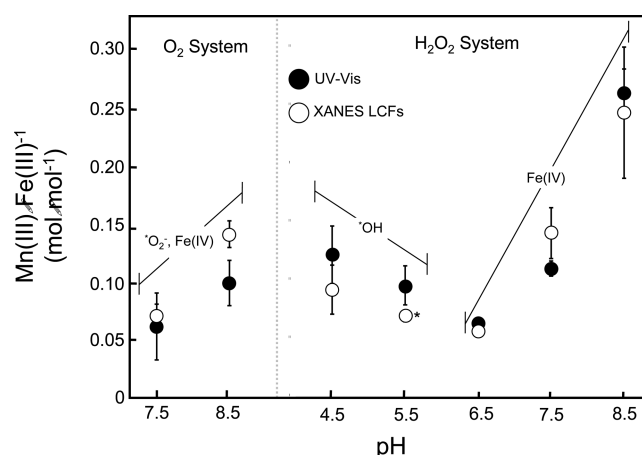


**Figure 3.** Effect of pH on the Mn(III)·Fe<sup>−1</sup> molar ratio of the reaction products generated in the EC–O<sub>2</sub> and EC–H<sub>2</sub>O<sub>2</sub> systems. Empty circles represent the results derived from Mn K-edge XANES LCFs, whereas filled circles indicate PP-extraction results. The asterisk indicates that for this data point, only Mn(II) removal is reported because XANES spectra were not collected for this sample. The data points for the pH 8.5 H<sub>2</sub>O<sub>2</sub> samples have been corrected for surface-catalyzed Mn(III) production. Error bars represent the standard deviation of average measurements (UV-vis) or the fit-derived error on Mn(III) fraction (XANES).

and  $91 \pm 7$  for EC–O<sub>2</sub> samples (IPR =  $5 \mu\text{M}\cdot\text{min}^{-1}$ ) generated at pH 7.5 and 8.5, respectively. In the EC–H<sub>2</sub>O<sub>2</sub> system, the percent Mn(III) ranged from  $74 \pm 17$  to  $80 \pm 5$  for experiments spanning pH values from 4.5 to 8.5. For some samples in the EC–O<sub>2</sub> or EC–H<sub>2</sub>O<sub>2</sub> systems, the LCFs produced small fractions of Mn(II) ( $<10\%$ ) and Mn(IV) ( $<15\%$ ), but the calculated standard deviation on these Mn(II) and Mn(IV) fractions was always larger than the fit-derived value (Figure S5). An exception was the sample generated in the EC–H<sub>2</sub>O<sub>2</sub> system at pH 8.5, which yielded a reproducible fit-derived Mn(II) fraction of  $7.8 \pm 0.5\%$ . The absence of significant fractions of Mn(IV) determined in the LCFs for all samples is consistent with the identical measurements of total Mn by ICP-OES before and after filtering the PP extractions because Mn(IV) in the solid phase would be removed by filtration in these experiments.<sup>46</sup>

**Fe K-Edge EXAFS Spectroscopy. Fe K-Edge EXAFS Spectra.** Figure 4A shows the Fe K-edge EXAFS spectra and corresponding Fourier transforms for samples generated in the EC–O<sub>2</sub> system (blue) at IPR values of 5 and  $50 \mu\text{M}\cdot\text{min}^{-1}$  and the EC–H<sub>2</sub>O<sub>2</sub> system (green) at an IPR of  $5 \mu\text{M}\cdot\text{min}^{-1}$ . The Fe K-edge EXAFS and Fourier transforms of two-line ferrihydrite and lepidocrocite ( $\gamma\text{-FeOOH}$ ) are also presented in Figure 4. For samples generated in the EC–O<sub>2</sub> system, no significant changes in line shape nor in the amplitude and phase of the EXAFS oscillations are observed with changes in IPR or pH. The EXAFS spectra of EC–O<sub>2</sub> samples show a close match to the lepidocrocite reference spectrum with respect to the first oscillation and the intensity and width of the oscillations at  $k > 8 \text{ \AA}^{-1}$ . In contrast, the EXAFS spectra of samples generated in the EC–H<sub>2</sub>O<sub>2</sub> system resemble strongly ferrihydrite, including the symmetric first oscillation and the lower intensity and broad oscillations at  $k > 8 \text{ \AA}^{-1}$ .

**Shell-by-Shell Fits.** Shell-by-shell fits of the Fe K-edge EXAFS spectra (Figure S9 and Table S2) of representative samples in the EC–O<sub>2</sub> and EC–H<sub>2</sub>O<sub>2</sub> systems (pH 7.5, IPR =  $5 \mu\text{M}\cdot\text{min}^{-1}$ ) are consistent with the formation of lepidocrocite

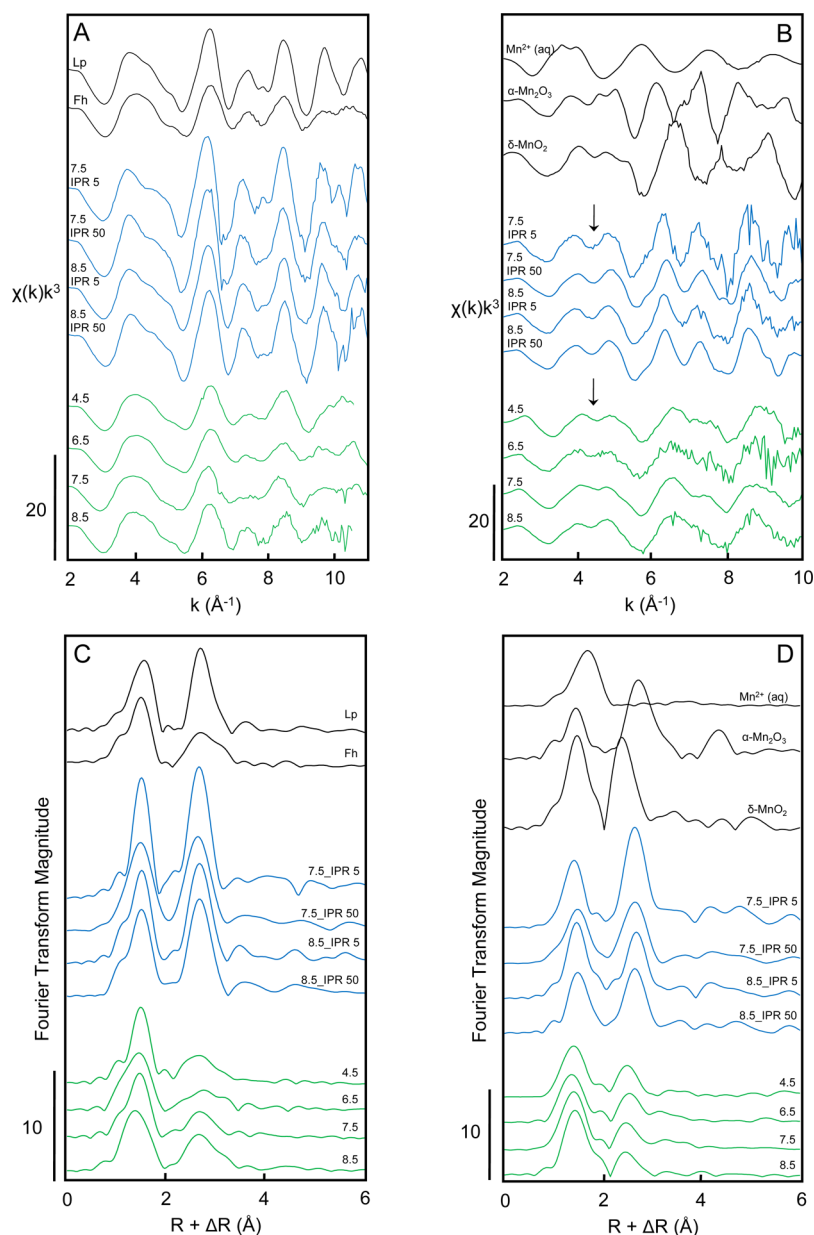


**Figure 4.** Fe (A) and Mn (B) K-edge EXAFS spectra and corresponding Fourier transforms (C and D). Samples generated in the EC–O<sub>2</sub> (blue) and EC–H<sub>2</sub>O<sub>2</sub> (green) systems are plotted below references (black). Samples for the EC–O<sub>2</sub> system were generated at IPR values of 5 or 50  $\mu\text{M}\cdot\text{min}^{-1}$ , whereas only samples generated at IPR = 5  $\mu\text{M}\cdot\text{min}^{-1}$  are given for the EC–H<sub>2</sub>O<sub>2</sub> system. The arrow in panel B highlights the doublet in the first oscillation of the Mn EXAFS spectra.

and poorly crystalline hydrous ferric oxide (HFO) when the initial Fe(II) oxidant was O<sub>2</sub> and H<sub>2</sub>O<sub>2</sub>, respectively. For samples generated in the EC–O<sub>2</sub> system, the fit returned values of  $R_{\text{Fe–O}} = 2.00 \pm 0.01$   $\text{\AA}$  and  $\text{CN}_{\text{Fe–O}} = 5.4 \pm 1.2$  for the first shell and  $R_{\text{Fe–Fe}} = 3.07 \pm 0.01$   $\text{\AA}$  and  $\text{CN}_{\text{Fe–Fe}} = 6.1 \pm 1.5$  for the second shell. These parameters indicate the presence of edge-sharing FeO<sub>6</sub> octahedra and are in excellent agreement with previous EXAFS fits and the crystal structure of lepidocrocite.<sup>36,41,54</sup> Although some subtle differences exist between the EXAFS spectra of EC–O<sub>2</sub> samples and the lepidocrocite reference, these differences are consistent with the formation of pseudo lepidocrocite in the EC–/O<sub>2</sub> system,<sup>41</sup> which is a lepidocrocite with poor sheet-stacking coherence often observed as the product of Fe(II) oxidation by O<sub>2</sub>.<sup>36</sup> For precipitates generated in the EC–H<sub>2</sub>O<sub>2</sub> system, shell-by-shell fits produced similar  $R$  values as those obtained in the EC–O<sub>2</sub>

system ( $R_{\text{Fe–O}} = 2.00 \pm 0.01$   $\text{\AA}$  and  $R_{\text{Fe–Fe}} = 3.08 \pm 0.01$   $\text{\AA}$ ), indicating the presence of edge-sharing FeO<sub>6</sub> octahedra, but the fit returned a substantially lower value of  $\text{CN}_{\text{Fe–Fe}}$  ( $3.0 \pm 0.4$ ). In addition, the fit did not support the presence of an Fe–Fe path corresponding to corner-sharing Fe polyhedra (failed test of statistical significance; see the [Supporting Information](#)). The weak intensity of the second-shell peak and the absence of significant fractions of corner-sharing Fe polyhedra are indicative of poorly crystalline HFO,<sup>36,41</sup> which is expected to form in the EC–H<sub>2</sub>O<sub>2</sub> system on the basis of the rapid rate of Fe(II) oxidation by H<sub>2</sub>O<sub>2</sub>.<sup>26,55</sup> The formation of lepidocrocite and HFO in the EC–O<sub>2</sub> and EC–H<sub>2</sub>O<sub>2</sub> systems, respectively, was also confirmed by XRD (Figure S7). Based on these results, we conclude that the major variable influencing the structure of the resulting Fe(III) phase is the Fe(II) oxidant, with pH and IPR playing a secondary role, if any.

**Mn K-Edge EXAFS Spectroscopy.** *Mn K-Edge EXAFS Spectra.* The Mn K-edge EXAFS spectra and Fourier transforms of samples generated in the EC–O<sub>2</sub> and EC–H<sub>2</sub>O<sub>2</sub> systems as well as spectra of aqueous Mn(II), bixbyite ( $\alpha$ -Mn<sub>2</sub>O<sub>3</sub>), and  $\delta$ -MnO<sub>2</sub> are shown in Figure 4B. Similar to the Fe K-edge EXAFS spectra, the Mn K-edge data are best grouped by the initial oxidant, with pH and IPR having a small impact on the local Mn coordination environment. The EXAFS spectra of EC–H<sub>2</sub>O<sub>2</sub> samples display substantially weaker oscillations at all *k*-values relative to those in the EC–O<sub>2</sub> system. This result indicates a similar but less-ordered average Mn bonding environment in the EC–H<sub>2</sub>O<sub>2</sub> samples relative to EC–O<sub>2</sub> samples. Not only do the EXAFS spectra of the EC–O<sub>2</sub> samples differ relative to those of the EC–H<sub>2</sub>O<sub>2</sub> samples, but also, all experimental spectra differ significantly from the Mn<sup>2+</sup> and  $\delta$ -MnO<sub>2</sub> reference spectra shown in Figure 4B as well as those from manganite ( $\alpha$ -MnOOH), groutite ( $\gamma$ -MnOOH), and feitknechtite ( $\gamma$ -MnOOH) (Figure S8). This latter set of references are the most-stable Mn(III)-bearing minerals that would form in these experiments.<sup>56,57</sup> Although the EXAFS spectra of the EC–O<sub>2</sub> experimental samples do show some similarity to the bixbyite EXAFS spectrum, the overlay of these two EXAFS spectra (Figure S8) reveals differences in the oscillations above *k* of 5.5 Å<sup>−1</sup>; these differences are clearly manifest in the shape of the second-shell peak of the Fourier transformed EXAFS spectrum (Figure 4D).

**Shell-by-Shell Fits.** Fits of the first-shell peak of representative samples in both EC–O<sub>2</sub> and EC–H<sub>2</sub>O<sub>2</sub> systems (pH 7.5, IPR = 5 μM·min<sup>−1</sup>) returned identical values for *R*<sub>Mn–O</sub> (1.91 ± 0.01 Å) and CN<sub>Mn–O</sub> (2.4–3.1), within the fit-derived error (Table S2). The presence of Jahn–Teller distorted Mn(III) in the samples is supported by the substantially lower fit-derived CN<sub>Mn–O</sub> values relative to the theoretical value of 6 for octahedral coordination<sup>54</sup> and is consistent with the weaker first-shell peak in the Fourier transformed EXAFS spectrum of bixbyite relative to that of  $\delta$ -MnO<sub>2</sub> (Figure 4D). Beyond the first Mn–O coordination shell, the EC–O<sub>2</sub> and EC–H<sub>2</sub>O<sub>2</sub> samples differ in terms of the amplitude of the second-shell peaks. Fits of this peak returned similar *R*<sub>Mn–Mn/Fe</sub> values of 3.04 ± 0.01 and 2.98 ± 0.03 Å for the EC–O<sub>2</sub> and EC–H<sub>2</sub>O<sub>2</sub> samples, respectively. Although these fit-derived distances do not match the *R*<sub>Mn–Mn</sub> values of edge-sharing MnO<sub>6</sub> octahedra in Mn(III) (oxyhydr)oxides (e.g., *R*<sub>Mn–Mn</sub> = 2.85 Å in groutite<sup>54</sup> and 3.11 Å in bixbyite<sup>58</sup>), they are similar to the *R*<sub>Fe–Fe</sub> values of edge-sharing FeO<sub>6</sub> octahedra in lepidocrocite (*R*<sub>Fe–Fe</sub> = 3.05–3.06 Å)<sup>54</sup> and ferrihydrite (*R*<sub>Fe–Fe</sub> = 2.94–3.02 Å).<sup>59</sup> In addition, the shell-by-shell fits returned substantially lower values for the disorder parameter ( $\sigma^2_{\text{Mn–Mn/Fe}}$ ) in the EC–O<sub>2</sub> sample (0.003 ± 0.002 Å<sup>2</sup>) relative to that of the EC–H<sub>2</sub>O<sub>2</sub> sample (0.016 ± 0.06 Å<sup>2</sup>). The more-ordered coordination environment of Mn in the EC–O<sub>2</sub> samples relative to the EC–H<sub>2</sub>O<sub>2</sub> samples mirrors the more ordered coordination environment of Fe in lepidocrocite relative to HFO. Although we cannot rule out the formation of a separate Mn(III) phase or surface precipitate, we argue against this interpretation because the Mn K-edge EXAFS spectra revealed that the EC–O<sub>2</sub> samples attained an ordered second-shell coordination environment, as reflected in the low  $\sigma^2$  values indicative of a single Mn–Mn/Fe distance. However, no perceptible Bragg diffraction peaks such as those that would arise from Mn(III)-bearing minerals were observed in the XRD data of EC samples (Figure S7). In addition, the absence of a shoulder at higher *R* in the second-shell peak of the Fourier

transformed EXAFS spectrum of the EC–O<sub>2</sub> samples indicates the lack of corner-sharing Mn–Mn/Fe linkages, which is inconsistent with the structure of bixbyite but consistent with structural incorporation into lepidocrocite.

## DISCUSSION

### Products of Fe(II)-Mediated Mn(II) Oxidation.

Manganese(II) oxidation in the EC–O<sub>2</sub> and EC–H<sub>2</sub>O<sub>2</sub> systems proceeds through a single electron transfer to generate Mn(III) as demonstrated by the PP extractions and Mn K-edge XANES analyses. The Mn K-edge EXAFS also show that the Mn-bonding environment in the EC samples differs substantially from that of crystalline Mn(III) (oxyhydr)oxide minerals. Instead, the second-shell peak position and amplitude of the Fourier transformed Mn K-edge EXAFS spectra mirrors that of the Fourier transformed Fe K-edge EXAFS spectra across all samples, despite variations in IPR, pH, and Mn(III)·Fe<sup>−1</sup> ratio. Therefore, we propose that Fe(II)-mediated Mn(II) oxidation produces Mn(III), which is stabilized by substitution for Fe(III) octahedra in the resulting Fe(III) coprecipitates (lepidocrocite in the EC–O<sub>2</sub> system, HFO in the EC–H<sub>2</sub>O<sub>2</sub> system). Although Mn(III) might also be adsorbed by the Fe(III) precipitates, we argue against this interpretation because surface-bound Mn would increase with increasing pH<sup>53</sup> and lead to a systematic decrease in the amplitude of the second shell peak of the Fourier transformed Mn K-edge EXAFS spectra with pH, which was not observed.

The formation of Mn(III)-substituted Fe(III)-bearing minerals in the EC system is supported by several laboratory-based studies that report the synthesis of Fe(III) (oxyhydr)oxide minerals (e.g., goethite) bearing up to 30 mol % Mn(III).<sup>60–63</sup> The favorable incorporation of Mn(III) in Fe(III) (oxyhydr)oxides, such as goethite, can be explained by the similar trivalent charge and size of Mn(III) and Fe(III) octahedra (average *R*<sub>Mn–O</sub> = 2.03 Å in groutite,<sup>54</sup> average *R*<sub>Fe–O</sub> = 2.03 Å in goethite<sup>51</sup>). However, Mn(III) octahedra can be significantly distorted, having a larger range of first-shell Mn–O distances (*R*<sub>Mn–O</sub> = 1.89–2.18 Å in groutite<sup>54</sup>) relative to Fe(III) octahedra (*R*<sub>Fe–O</sub> = 1.93–2.13 Å in goethite<sup>51</sup>). This difference in *R*<sub>Mn–O</sub> and *R*<sub>Fe–O</sub> distances, particularly the shorter Mn–O bond lengths of equatorial oxygens,<sup>64,65</sup> can explain the small decrease in bond length of the next-nearest neighbor Mn shell (*R*<sub>Mn–Mn/Fe</sub> = 2.98–3.04 Å) relative to that of Fe (*R*<sub>Fe–Fe</sub> = 3.07–3.08 Å) in the EC samples (Table S2).

**Controls on Mn(II) Oxidation Efficiency. Iron Production Rate.** The removal of Mn(II) from solution increased with decreasing IPR for a range of EC–O<sub>2</sub> and EC–H<sub>2</sub>O<sub>2</sub> samples, with the largest effect observed in the EC–O<sub>2</sub> system at pH 7.5 (Figure 2). At this pH, we found no heterogeneous Mn(II) oxidation. In addition, the solid-phase Mn and Fe speciation was similar at low and high IPR values. Therefore, the enhanced removal of Mn(II) at lower IPR, particularly in the EC–O<sub>2</sub> system at pH 7.5, is best-explained by the competition of Fe(II) and Mn(II) for the reactive intermediates generated in Fenton type systems. As shown in Figure 1, the oxidation of Fe(II) by O<sub>2</sub> or H<sub>2</sub>O<sub>2</sub> yields Fenton type products that can oxidize Mn(II) or be quenched by direct reaction with Fe(II). In addition, Mn(III) can be reduced back to Mn(II) rapidly (seconds to minutes) by aqueous Fe(II).<sup>66</sup> Although rapid, the rate of Fe(II) oxidation by O<sub>2</sub> at pH 7.5 can be slower than the rate of Fe(II) addition at high IPR values<sup>29,42</sup> and thus lead to the accumulation of aqueous Fe(II), which is consistent with previous work in the EC–O<sub>2</sub> system.<sup>29</sup> Therefore, to optimize



the efficiency of Fe(II)-mediated Mn(II) oxidation, it is critical to balance the rate of Fe(II) addition by EC and the rate of Fe(II) oxidation. In contrast, Fe(II) oxidation by  $O_2$  at pH 8.5 (and by  $H_2O_2$  at all pH values) is orders of magnitude faster than at pH 7.5.<sup>26,42</sup> Therefore, the consumption of reactive oxidants due to the accumulation of aqueous Fe(II) is not a concern at pH values greater than 7.5.

**Solution pH.** The efficiency of Fe(II)-mediated Mn(II) oxidation increased in the EC- $O_2$  and EC- $H_2O_2$  systems as pH increased from 6.5 to 8.5 (Figure 2) and as pH decreased from 6.5 to 4.5 in the EC- $H_2O_2$  system. However, solution pH did not modify the bonding environment of Fe and Mn in the reaction products. Therefore, the trends in the pH dependence of Fe(II)-mediated Mn(II) oxidation can be explained by (i) a change in the aqueous speciation of Fe(II) and Mn(II) from pH 6.5 to 8.5 (Figure S10) and (ii) a transition in the identity of the reactive oxidant responsible for Mn(II) oxidation from pH 6.5 to 4.5. As pH increases from neutral to mildly alkaline, the fraction of the free metal ions ( $Fe^{2+}$  and  $Mn^{2+}$ ) decreases in favor of hydrolysis species and metal-carbonate complexes, which have orders of magnitude faster oxidation rates than their free-ion counterparts.<sup>16,17,42</sup> Consequently, an increase in pH from 6.5 to 8.5 enhances Mn(II) oxidation kinetics due to changes in aqueous Mn(II) speciation and by increasing the rate of Fe(II) oxidation, which eliminates the accumulation of aqueous Fe(II) and reduces the competition between Fe(II) and Mn(II) for reactive oxidants.

As pH decreases from 6.5 to 4.5, no significant change in Fe(II) or Mn(II) aqueous speciation occurs (Figure S10). However, within this pH range, the intermediate oxidant produced from the Fenton reaction (INT in Figure 1) transitions from a less-powerful oxidant (presumably Fe(IV)) to  $\cdot OH$ ,<sup>26</sup> which oxidizes Mn(II) at a rate that is orders of magnitude faster than Fe(IV).<sup>25,67</sup> This transition to the production of  $\cdot OH$  at acidic pH is gradual, with complete production of  $\cdot OH$  likely occurring at pH values of <5.5,<sup>26,28</sup> which is consistent with the increase in Mn(II) oxidation efficiency in the EC- $H_2O_2$  system as pH decreases from 6.5 to 4.5. Based on this interpretation, we have delineated the pH regimes in which  $\cdot OH$  and presumably Fe(IV) are the dominant Mn(II) oxidants in Figure 3.

**Fe(II) Oxidant.** For a given solution pH and IPR value, the yield of Mn(III) in the reaction products is higher when Fe(II) is oxidized in the EC system by  $H_2O_2$  rather than  $O_2$  (Figure 2). This result can be explained by three processes. First, the rate of Fe(II) oxidation is significantly higher in the presence of  $H_2O_2$  than in the presence of  $O_2$ ,<sup>26</sup> which prevents the buildup of aqueous Fe(II) and thereby decreases the competition between Fe(II) and Mn(II) for Fenton products. Second, the presence of  $H_2O_2$  leads to more efficient yields of INT (1:1 ratio of Fe(II) oxidized per INT formed; see Figure 1) than if INT production was initiated by Fe(II) reactions with  $O_2$  (3:1 ratio of Fe(II) oxidized per INT formed). Although both  $\cdot O_2^-$  and INT can oxidize Mn(II), the enhanced Mn(II) oxidation in the EC- $H_2O_2$  system relative to the EC- $O_2$  system at identical IPR and solution pH supports the primary role of INT as the Fe(II)-mediated Mn(II) oxidant. Third, in contrast to the effects of IPR and pH on the reaction mechanism, the identity of the Fe(II) oxidant determined the structure of the solid-phase hosting Mn(III). As shown in Figure 4C, the HFO generated in the EC- $H_2O_2$  system bears considerably more structural disorder than the moderately crystalline lepidocrocite produced in EC- $O_2$  system. This result is consistent with the

rapid oxidation of Fe(II) by  $H_2O_2$  and presumably rapid incorporation of Mn(III), which would otherwise disproportionate to Mn(II) and Mn(IV). We expect that the formation of HFO favors more efficient yields of Mn(III) due to the ability of poorly crystalline, disordered solids to accommodate higher fractions of foreign ions in their structure than crystalline minerals.<sup>68</sup>

**Technical and Environmental Implications.** *Mn(II) as a Sink of Reactive Oxidants.* Fenton type reactions involving the oxidation of Fe(II) by  $O_2$  or  $H_2O_2$  are exploited extensively to oxidize target contaminants and are important in the environmental fate of redox active elements (e.g., As(III) and Sb(III)) and organic carbon.<sup>26,28,33,34</sup> We show that Fenton type reactions unleashed via Fe(0) EC also oxidize Mn(II) efficiently (0.02 to >0.2 Mn(III)·Fe<sup>-1</sup>), with key roles being played by the IPR, solution pH, and the presence of  $H_2O_2$ . Our results demonstrate that Fe(0) EC can be a viable method to prevent exposure to Mn(II) in drinking water, especially in decentralized areas where the modular properties and low supply infrastructure of EC systems provide advantages over conventional technologies.<sup>69,70</sup> Our work also shows that Mn(II) is an important sink of reactive oxidants that must be considered for accurate predictions of Fe(II)-mediated oxidation of redox active species. For example, low-cost Fe-based techniques to remove As(III) from contaminated groundwater, which often contains considerably higher levels of Mn(II) relative to As(III),<sup>71,72</sup> typically rely on the oxidation of As(III) to the less-toxic and readily sorbed As(V) oxyanion.<sup>35,37</sup> Comparisons between our results and those reported previously for As(III) oxidation in the Fe(0) EC system<sup>29</sup> suggest that Mn(II) can compete with As(III) for Fenton products. The competition between Mn(II) and As(III) for reactive oxidants, which would decrease As(III) removal efficiency, is also consistent with Fe(0) EC field studies that report poorer As removal performance in natural groundwater containing significant Mn(II) concentrations<sup>73</sup> relative to laboratory-based experiments performed in Mn(II)-free synthetic groundwater.<sup>35</sup>

**Reactivity of Mn(III)-Bearing Fe(III) Precipitates Generated in Fenton Type Systems.** Our results show that Fe(II)-mediated Mn(II) oxidation produces Mn(III) that is stabilized against disproportionation via structural incorporation into coprecipitated Fe(III) solids. The formation of Mn(III) is particularly relevant to the ensuing reactivity of the solid phase given its strong oxidation potential. For example, Mn(III)-incorporated goethites (0.1 mol·mol<sup>-1</sup>) oxidize As(III) effectively, whereas Mn(III)-free goethites were found to be unreactive.<sup>63</sup> Recent evidence also shows that the oxidation of inorganic<sup>74,75</sup> and organic<sup>76</sup> species by Mn(IV) oxides can be linked to the availability of Mn(III) at the oxide surface. Furthermore, at near-neutral pH, Fenton type reactions produce a selective oxidant, presumably Fe(IV),<sup>26</sup> that is weaker than  $\cdot OH$  and can be less-reactive with persistent organic compounds than oxidized Mn(III/IV).<sup>10</sup> Therefore, we speculate that the presence of Mn(II) in Fenton type systems at near-neutral pH may act as a catalyst to oxidize compounds that are unreactive with Fe(IV) via Mn(III) intermediates.

## ■ ASSOCIATED CONTENT

### Supporting Information

The Supporting Information is available free of charge on the ACS Publications website at DOI: 10.1021/acs.est.6b05584.

Additional details of the pyrophosphate extractions, XAS and XRD results, and speciation calculations. (PDF)

## AUTHOR INFORMATION

### Corresponding Author

\*E-mail: [jasquelin.pena@unil.ch](mailto:jasquelin.pena@unil.ch).

### ORCID

Jasquelin Peña: 0000-0001-7081-3873

### Notes

The authors declare no competing financial interest.

## ACKNOWLEDGMENTS

This work was funded by the Swiss National Science Foundation (200021\_169555), The Sandoz Family Foundation and BCV Foundation. CVG acknowledges funding from the Netherlands Organisatie voor Wetenschappelijk Onderzoek. Experiments were performed on beamline BM-01 and BM-23 at the European Synchrotron Radiation Facility (ESRF), Grenoble, France. We are grateful to Michaela Brunelli (BM-01), Hermann Emerich (BM-01), and Vera Cuartero (BM-23) at the ESRF for providing assistance. We also thank Ryan Davis, Sharon Bone, and Francesco Marafatto for technical support during data collection at the Stanford Synchrotron Radiation Lightsource. Use of the Stanford Synchrotron Radiation Lightsource, SLAC National Accelerator Laboratory, is supported by the U.S. Department of Energy, Office of Science, Office of Basic Energy Sciences under Contract No. DE-AC02-76SF00515.

## REFERENCES

- (1) Kohl, P. M.; Medlar, S. J.; AWWA Research Foundation; Environmental Protection Agency. *Occurrence of Manganese in Drinking Water and Manganese Control*; AWWA Research Foundation/American Water Works Association/IWA Publications: Denver, CO, 2006; p. 184.
- (2) BGS. *Arsenic contamination of groundwater in Bangladesh*; British Geological Survey: Nottingham, U.K., 2001.
- (3) Katsoyiannis, I. A.; Zouboulis, A. I. Biological treatment of Mn(II) and Fe(II) containing groundwater: kinetic considerations and product characterization. *Water Res.* **2004**, *38* (7), 1922–1932.
- (4) USEPA. *National Secondary Drinking Water Regulations*; USEPA: Washington, DC, 1979.
- (5) WHO. *Manganese in Drinking-water: Background document for development of WHO Guidelines for Drinking-water Quality*; WHO: Geneva, Switzerland, 2011.
- (6) Charlet, L.; Chapron, Y.; Faller, P.; Kirsch, R.; Stone, A.; Baveye, P. Neurodegenerative diseases and exposure to the environmental metals Mn, Pb, and Hg. *Coord. Chem. Rev.* **2012**, *256* (19–20), 2147–2163.
- (7) Wasserman, G.; Liu, X.; Parvez, F.; Ahsan, H.; Levy, D.; Factor-Litvak, P.; Kline, J.; van Geen, A.; Slavkovich, V.; Lolacono, N.; Cheng, Z.; Zheng, Y.; Graziano, J. Water manganese exposure and children's intellectual function in Araihaazar, Bangladesh. *Environ. Health Perspect.* **2005**, *114* (1), 124–129.
- (8) Bouchard, M.; Sauve, S.; Barbeau, B.; Legrand, M.; Brodeur, M.; Bouffard, T.; Limoges, E.; Bellingier, D.; Mergler, D. Intellectual Impairment in School-Age Children Exposed to Manganese from Drinking Water. *Environ. Health Perspect.* **2010**, *119* (1), 138–143.
- (9) Tebo, B.; Bargar, J.; Clement, B.; Dick, G.; Murray, K.; Parker, D.; Verity, R.; Webb, S. Biogenic manganese oxides: Properties and mechanisms of formation. *Annu. Rev. Earth Planet. Sci.* **2004**, *32*, 287–328.
- (10) Remucal, C.; Ginder-Vogel, M. A critical review of the reactivity of manganese oxides with organic contaminants. *Environ. Sci. Process. Impacts* **2014**, *16* (6), 1247–1266.
- (11) Manning, B. A.; Fendorf, S. E.; Bostick, B.; Suarez, D. L. Arsenic(III) oxidation and arsenic(V) adsorption reactions on synthetic birnessite. *Environ. Sci. Technol.* **2002**, *36* (5), 976–981.
- (12) Borch, T.; Kretzschmar, R.; Kappler, A.; Van Cappellen, P.; Ginder-Vogel, M.; Voegelin, A.; Campbell, K. Biogeochemical Redox Processes and their Impact on Contaminant Dynamics. *Environ. Sci. Technol.* **2010**, *44* (1), 15–23.
- (13) Learman, D.; Voelker, B.; Madden, A.; Hansel, C. Constraints on superoxide mediated formation of manganese oxides. *Front. Microbiol.* **2013**, *4*, 10.3389/fmicb.2013.00262
- (14) Learman, D.; Wankel, S.; Webb, S.; Martinez, N.; Madden, A.; Hansel, C. Coupled biotic-abiotic Mn(II) oxidation pathway mediates the formation and structural evolution of biogenic Mn oxides. *Geochim. Cosmochim. Acta* **2011**, *75* (20), 6048–6063.
- (15) Nico, P.; Anastasio, C.; Zasoski, R. Rapid photo-oxidation of Mn(II) mediated by humic substances. *Geochim. Cosmochim. Acta* **2002**, *66* (23), 4047–4056.
- (16) Morgan, J. Kinetics of reaction between O<sub>2</sub> and Mn(II) species in aqueous solutions. *Geochim. Cosmochim. Acta* **2005**, *69* (1), 35–48.
- (17) Sung, W.; Morgan, J. Oxidative removal of Mn(II) from solution catalyzed by the gamma-FeOOH (lepidocrocite) surface. *Geochim. Cosmochim. Acta* **1981**, *45* (12), 2377–2383.
- (18) Doula, M. Removal of Mn<sup>2+</sup> ions from drinking water by using Clinoptilolite and a Clinoptilolite-Fe oxide system. *Water Res.* **2006**, *40* (17), 3167–3176.
- (19) Choo, K.; Lee, H.; Choi, S. Iron and manganese removal and membrane fouling during UF in conjunction with prechlorination for drinking water treatment. *J. Membr. Sci.* **2005**, *267* (1–2), 18–26.
- (20) Reisz, E.; Leitzke, A.; Jarocki, A.; Irmischer, R.; von Sonntag, C. Permanganate formation in the reactions of ozone with Mn(II): a mechanistic study. *Aqua* **2008**, *57* (6), 451–464.
- (21) von Gunten, U. Ozonation of drinking water: Part I. Oxidation kinetics and product formation. *Water Res.* **2003**, *37* (7), 1443–1467.
- (22) Andeer, P.; Learman, D.; McIlvin, M.; Dunn, J.; Hansel, C. Extracellular haem peroxidases mediate Mn(II) oxidation in a marine *Roseobacter* bacterium via superoxide production. *Environ. Microbiol.* **2015**, *17* (10), 3925–3936.
- (23) Learman, D.; Voelker, B.; Vazquez-Rodriguez, A.; Hansel, C. Formation of manganese oxides by bacterially generated superoxide. *Nat. Geosci.* **2011**, *4* (2), 95–98.
- (24) Baral, S.; Lumepeira, C.; Janata, E.; Henglein, A. Chemistry of colloidal Manganese oxides. 3. Formation in the reaction of hydroxyl radicals with Mn<sup>2+</sup> ions. *J. Phys. Chem.* **1986**, *90* (22), 6025–6028.
- (25) Jacobsen, F.; Holcman, J.; Sehested, K. Reactions of the ferryl ion with some compounds found in cloud water. *Int. J. Chem. Kinet.* **1998**, *30* (3), 215–221.
- (26) Hug, S. J.; Leupin, O. Iron-catalyzed oxidation of arsenic(III) by oxygen and by hydrogen peroxide: pH-dependent formation of oxidants in the Fenton reaction. *Environ. Sci. Technol.* **2003**, *37* (12), 2734–2742.
- (27) Pereira, M.; Oliveira, L.; Murad, E. Iron oxide catalysts: Fenton and Fenton-like reactions - a review. *Clay Miner.* **2012**, *47* (3), 285–302.
- (28) Leuz, A.; Hug, S.; Wehrli, B.; Johnson, C. Iron-mediated oxidation of antimony(III) by oxygen and hydrogen peroxide compared to arsenic(III) oxidation. *Environ. Sci. Technol.* **2006**, *40* (8), 2565–2571.
- (29) Li, L.; van Genuchten, C. M.; Addy, S. E. A.; Yao, J.; Gao, N.; Gadgil, A. J. Modeling As(III) oxidation and removal with iron electrocoagulation in groundwater. *Environ. Sci. Technol.* **2012**, *46* (21), 12038–12045.
- (30) Watts, R.; Dilly, S. Evaluation of iron catalysts for the Fenton-like remediation of diesel-contaminated soils. *J. Hazard. Mater.* **1996**, *51* (1–3), 209–224.
- (31) Watts, R.; Teel, A. Chemistry of modified Fenton's reagent (catalyzed H<sub>2</sub>O<sub>2</sub> propagations-CHP) for in situ soil and groundwater remediation. *J. Environ. Eng.* **2005**, *131* (4), 612–622.
- (32) Kim, J.; Lee, C.; Sedlak, D.; Yoon, J.; Nelson, K. Inactivation of MS2 coliphage by Fenton's reagent. *Water Res.* **2010**, *44*, 2647–2653.



- (33) Page, S.; Sander, M.; Arnold, W.; McNeill, K. Hydroxyl Radical Formation upon Oxidation of Reduced Humic Acids by Oxygen in the Dark. *Environ. Sci. Technol.* **2012**, *46* (3), 1590–1597.
- (34) Hall, S.; Silver, W. Iron oxidation stimulates organic matter decomposition in humid tropical forest soils. *Glob. Chang. Biol.* **2013**, *19* (9), 2804–2813.
- (35) van Genuchten, C.; Addy, S.; Pena, J.; Gadgil, A. Removing arsenic from synthetic groundwater with iron electrocoagulation: An Fe and As K-edge EXAFS study. *Environ. Sci. Technol.* **2012**, *46* (2), 986–994.
- (36) Voegelin, A.; Kaegi, R.; Frommer, J.; Vantelon, D.; Hug, S. J. Effect of phosphate, silicate, and Ca on Fe(III)-precipitates formed in aerated Fe(II)- and As(III)-containing water studied by X-ray absorption spectroscopy. *Geochim. Cosmochim. Acta* **2010**, *74* (1), 164–186.
- (37) Neumann, A.; Kaegi, R.; Voegelin, A.; Hussam, A.; Munir, A.; Hug, S. Arsenic Removal with Composite Iron Matrix Filters in Bangladesh: A Field and Laboratory Study. *Environ. Sci. Technol.* **2013**, *47* (9), 4544–4554.
- (38) Dixit, S.; Hering, J. G. Comparison of arsenic(V) and arsenic(III) sorption onto iron oxide minerals: Implications for arsenic mobility. *Environ. Sci. Technol.* **2003**, *37* (18), 4182–4189.
- (39) Lakshmanan, D.; Clifford, D. A.; Samanta, G. Ferrous and Ferric Ion Generation During Iron Electrocoagulation. *Environ. Sci. Technol.* **2009**, *43* (10), 3853–3859.
- (40) van Genuchten, C. M.; Gadgil, A. J.; Peña, J. Fe(III) nucleation in the presence of bivalent cations and oxyanions leads to subnanoscale 7 Å polymers. *Environ. Sci. Technol.* **2014**, *48* (20), 11828–11836.
- (41) van Genuchten, C. M.; Peña, J.; Amrose, S. E.; Gadgil, A. J. Structure of Fe(III) precipitates generated by the electrolytic dissolution of Fe(0) in the presence of groundwater ions. *Geochim. Cosmochim. Acta* **2014**, *127*, 285–304.
- (42) Stumm, W.; Lee, G. Oxygenation of ferrous iron. *Ind. Eng. Chem.* **1961**, *53* (2), 143–146.
- (43) Morgan, B.; Lahav, O. The effect of pH on the kinetics of spontaneous Fe(II) oxidation by O<sub>2</sub> in aqueous solution - basic principles and a simple heuristic description. *Chemosphere* **2007**, *68* (11), 2080–2084.
- (44) Roberts, L. C.; Hug, S. J.; Ruettimann, T.; Billah, M.; Khan, A. W.; Rahman, M. T. Arsenic removal with iron(II) and iron(III) in waters with high silicate and phosphate concentrations. *Environ. Sci. Technol.* **2004**, *38* (1), 307–315.
- (45) Cornell, R. M.; Schwertmann, U. *The Iron Oxides: Structure, Properties, Reactions, Occurrence, and Uses*; VCH: Weinheim, NY, 1996; p 573.
- (46) Marafatto, F.; Strader, M.; Gonzalez-Holguera, J.; Schwartzberg, A.; Gilbert, B.; Pena, J. Rate and mechanism of the photoreduction of birnessite (MnO<sub>2</sub>) nanosheets. *Proc. Natl. Acad. Sci. U. S. A.* **2015**, *112* (15), 4600–4605.
- (47) Webb, S. M. SIXpack: a graphical user interface for XAS analysis using IFEFFIT. *Phys. Scr.* **2005**, *T115*, 1011–1014.
- (48) Manceau, A.; Marcus, M.; Grangeon, S. Determination of Mn valence states in mixed-valent manganates by XANES spectroscopy. *Am. Mineral.* **2012**, *97* (5–6), 816–827.
- (49) Newville, M. IFEFFIT: interactive XAFS analysis and FEFF fitting. *J. Synchrotron Radiat.* **2001**, *8*, 322–324.
- (50) Rehr, J.; Albers, R.; Zabinsky, S. High-order multiple-scattering calculations of X-ray absorption fine structure. *Phys. Rev. Lett.* **1992**, *69*, 3397–3400.
- (51) Gualtieri, A.; Venturelli, P. In situ study of the goethite-hematite phase transformation by real time synchrotron powder diffraction. *Am. Mineral.* **1999**, *84*, 895–904.
- (52) Lanson, B.; Drits, V.; Feng, Q.; Manceau, A. Structure of synthetic Na-birnessite: Evidence for a triclinic one-layer unit cell. *Am. Mineral.* **2002**, *87* (11–12), 1662–1671.
- (53) Davies, S.; Morgan, J. Manganese(II) Oxidation-Kinetics on Metal-Oxide Surfaces. *J. Colloid Interface Sci.* **1989**, *129* (1), 63–77.
- (54) Wyckoff, R. W. G. *Crystal Structures*; Interscience Publishers: New York, NY, 1963; Vol. 1, pp 290–295.
- (55) Katsoyiannis, I. A.; Ruettimann, T.; Hug, S. J. pH dependence of Fenton reagent generation and As(III) oxidation and removal by corrosion of zero valent iron in aerated water. *Environ. Sci. Technol.* **2008**, *42* (19), 7424–7430.
- (56) Junta, J.; Hochella, M. Manganese(II) Oxidation at Mineral Surfaces - A Microscopic and Spectroscopic Study. *Geochim. Cosmochim. Acta* **1994**, *58* (22), 4985–4999.
- (57) JuntaRosso, J.; Hochella, M.; Rimstidt, J. D. Linking microscopic and macroscopic data for heterogeneous reactions illustrated by the oxidation of manganese(II) at mineral surfaces. *Geochim. Cosmochim. Acta* **1997**, *61* (1), 149–159.
- (58) Geller, S. Structures of Alpha-Mn<sub>2</sub>O<sub>3</sub>(Mn<sub>0.983</sub>Fe<sub>0.017</sub>)<sub>2</sub>O<sub>3</sub> and (Mn<sub>0.37</sub>Fe<sub>0.63</sub>)<sub>2</sub>O<sub>3</sub> and Relation to Magnetic Ordering. *Acta Crystallogr., Sect. B: Struct. Crystallogr. Cryst. Chem.* **1971**, *27*, 821–828.
- (59) Michel, F. M.; Ehm, L.; Antao, S. M.; Lee, P. L.; Chupas, P. J.; Liu, G.; Strongin, D. R.; Schoonen, M. A. A.; Phillips, B. L.; Parise, J. B. The structure of ferrihydrite, a nanocrystalline material. *Science* **2007**, *316* (5832), 1726–1729.
- (60) Alvarez, M.; Rueda, E.; Sileo, E. Structural characterization and chemical reactivity of synthetic Mn-goethites and hematites. *Chem. Geol.* **2006**, *231* (4), 288–299.
- (61) Alvarez, M.; Rueda, E.; Sileo, E. Simultaneous incorporation of Mn and Al in the goethite structure. *Geochim. Cosmochim. Acta* **2007**, *71* (4), 1009–1020.
- (62) Alvarez, M.; Sileo, E.; Rueda, E. Effect of Mn(II) incorporation on the transformation of ferrihydrite to goethite. *Chem. Geol.* **2005**, *216* (1–2), 89–97.
- (63) Sun, X.; Doner, H. E.; Zavarin, M. Spectroscopy study of arsenite [As(III)] oxidation on Mn-substituted goethite. *Clays Clay Miner.* **1999**, *47* (4), 474–480.
- (64) Ebinger, M. H.; Schulze, D. G. Mn-Substituted Goethite and Fe-Substituted Groutite Synthesized at Acid pH. *Clays Clay Miner.* **1989**, *37* (2), 151–156.
- (65) Glasser, L.; Ingram, L. Refinement of Crystal Structure of Groutite Alpha-MnOOH. *Acta Crystallogr., Sect. B: Struct. Crystallogr. Cryst. Chem.* **1968**, *24*, 1233–1236.
- (66) Kostka, J.; Luther, G.; Nealson, K. Chemical and biological reduction of Mn(III)-pyrophosphate complexes - Potential importance of dissolved Mn(III) as an environmental oxidant. *Geochim. Cosmochim. Acta* **1995**, *59* (5), 885–894.
- (67) Buxton, G.; Greenstock, C.; Helman, W.; Ross, A. Critical-Review of Constants for Reactions of Hydrated Electrons, Hydrogen-Atoms and Hydroxyl Radicals (·OH/·O<sup>-</sup>) in Aqueous Solution. *J. Phys. Chem. Ref. Data* **1988**, *17* (2), 513–886.
- (68) Waychunas, G.; Kim, C.; Banfield, J. Nanoparticulate iron oxide minerals in soils and sediments: unique properties and contaminant scavenging mechanisms. *J. Nanopart. Res.* **2005**, *7*, 409–433.
- (69) Amrose, S. E.; Burt, Z.; Ray, I. Safe Drinking Water for Low-Income Regions. *Annu. Rev. Env. Resour.* **2015**, *40* (9), 203–231.
- (70) Gadgil, A. J.; Amrose, S. E.; Bandaru, S. R. S.; Delaire, C.; Torkelson, A. A.; van Genuchten, C. M. Addressing arsenic mass poisoning in South Asia with Electro-chemical arsenic remediation (ECAR). *Water Reclam. Sustainability* **2013**, 115.
- (71) Buschmann, J.; Berg, M.; Stengel, C.; Sampson, M. Arsenic and manganese contamination of drinking water resources in Cambodia: Coincidence of risk areas with low relief topography. *Environ. Sci. Technol.* **2007**, *41* (7), 2146–2152.
- (72) Biswas, A.; Nath, B.; Bhattacharya, P.; Halder, D.; Kundu, A.; Mandal, U.; Mukherjee, A.; Chatterjee, D.; Jacks, G. Testing Tubewell Platform Color as a Rapid Screening Tool for Arsenic and Manganese in Drinking Water Wells. *Environ. Sci. Technol.* **2012**, *46* (1), 434–440.
- (73) van Genuchten, C. M.; Bandaru, S. R. S.; Surorova, E.; Amrose, S. E.; Gadgil, A. J.; Pena, J. Formation of macroscopic surface layers on Fe(0) electrocoagulation electrodes during an extended field trial of arsenic treatment. *Chemosphere* **2016**, *153*, 270–279.

(74) Simanova, A. A.; Pena, J. Time-resolved investigation of cobalt oxidation by Mn(III)-rich  $\delta$ -MnO<sub>2</sub> using quick X-ray absorption spectroscopy. *Environ. Sci. Technol.* **2015**, *49*, 10867.

(75) Nico, P.; Zasoski, R. Importance of Mn(III) availability on the rate of Cr(III) oxidation on delta-MnO<sub>2</sub>. *Environ. Sci. Technol.* **2000**, *34* (16), 3363–3367.

(76) Nico, P.; Zasoski, R. Mn (III) center availability as a rate controlling factor in the oxidation of phenol and sulfide on delta-MnO<sub>2</sub>. *Environ. Sci. Technol.* **2001**, *35* (16), 3338–3343.